CHEMISTRY OF MATERIALS

pubs.acs.org/cm

Article

Evolution of Structural Order and Magnetic Anisotropy in $Yb_{0.5}(Co_{1-x}Fe_x)_3Ge_3$ through Doping of a Kagome Lattice

Rahul Meduri, Mario A. Plata, Gregory T. McCandless, Benny C. Schundelmier, Mehak Ghafoor, Kaya Wei, and Julia Y. Chan*

Cite This: *Chem. Mater.* 2025, 37, 2302−2313

Read Online

ACCESS | Metrics & More | Article Recommendations | Supporting Information

ABSTRACT: Kagome materials provide fruitful grounds for exploring the intersection of topology and magnetism. In this article, the single crystal growth of $Yb_{0.5}(Co_{1-x}Fe_x)_3Ge_3$ (x = 0.00, 0.25, 0.50, 0.75, and 1.00) is reported. As Fe is substituted into the Co-containing kagome net, the structure transforms from the disordered $Y_{0.5}Co_3Ge_3$/CoSn-type hybrid structure to the ordered $HfFe_6Ge_6$-type structure. Diffusive scattering is observed in all doped concentrations that eventually converge to a single reflection in the Fe end member, ultimately doubling the unit cell along the c-axis. Anisotropic magnetic measurements were performed to evaluate how the magnetism of the kagome lattice is influenced by Fe substitution. Magnetic interactions are primarily observed along the c-axis. Additionally, a reorientation of the magnetic easy axis is observed with increasing Fe incorporation, highlighting how the magnetism of this material can be chemically tuned. Resistivity with unusual behavior observed in the doped compositions is also reported. The rationale behind the structural evolution from disordered to ordered is discussed.

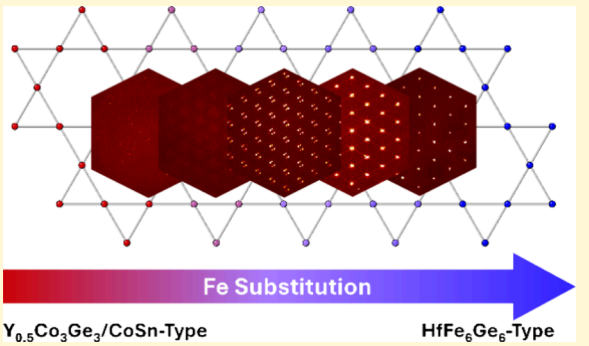

INTRODUCTION

Materials with a kagome sublattice consisting of a transition metal have sparked much interest in the condensed matter community due to the exotic quantum states and various topological band features present.[1,2] The AV_3Sb_5 (A = K, Rb, and Cs) family of compounds[3] has displayed charge density waves (CDWs),[4] superconductivity,[5] and an anomalous Hall effect.[6,7] The CDWs in CsV_3Sb_5 have been associated with an orthorhombic distortion of the kagome lattice, resulting in the doubling of the unit cell.[8,9] Alternatively, the mechanisms for CDWs observed in FeGe have shown to be primarily separate from the kagome net.[10,11] Annealing studies of FeGe show that the decrease in disordered structural features promotes CDW formation.[12] Fe_3Sn_2 has displayed room temperature skyrmions and an anomalous Hall effect.[13,14] $Co_3Sn_2S_2$ is a ferromagnet (Curie temperature = 180 K) that has also displayed a large anomalous Hall effect caused by magnetic Weyl Fermions positioned near the Fermi level.[15−17]

Members of the intermetallic AM_6X_6 (A = electropositive element, M = transition metal, X = main group element) family are another group of kagome materials that host a diverse array of electronic interactions that are fruitful in realizing new technologies, often owing to the strong exchange interaction of the rare-earth element and the transition metal.[18] ScV_6Sn_6 and $LuNb_6Sn_6$ have both shown density wave ordering.[19,20] A rattling mode of elements occupying the c-axis was proposed to be the mechanism behind charge ordering. A study that doped Sc with the larger Y and Lu shows that with increasing chemical pressure along the c-axis, the CDW transition is suppressed.[21] AM_6X_6 compounds where M = Mn, Fe are the only analogs to have been reported to possess high-temperature magnetic ordering in the kagome lattice[22] and give way to complex long-range magnetic structures, namely, with M = Mn.[23−26] Figure 1 shows the structure of $Yb_{0.5}Co_3Ge_3$, a disordered variant of compounds in the AM_6X_6 family that adopts a hybrid of the two structure types, $Y_{0.5}Co_3Ge_3$ and CoSn, that our group previously reported.[27] A Curie−Weiss fit to the magnetic susceptibility yielded an effective moment (μ_{eff}) of 4.23 μ_B with negative Weiss constants and no long-range magnetic ordering above 2 K, suggesting magnetic frustration. A higher magnetization was observed for H/c, giving rise to anisotropic magnetism within this compound. A feature around 25 K was also observed in the H // a data reminiscent of spin-canting or that a spin reorientation has occurred.[27] Data collection at 50 K revealed superlattice reflections warranting a doubling of the c-axis and a change in space group from $P6/mmm$ to $P6_3/m$.[28] Unlike the

Received: January 15, 2025
Revised: February 27, 2025
Accepted: February 28, 2025
Published: March 7, 2025

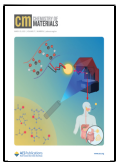

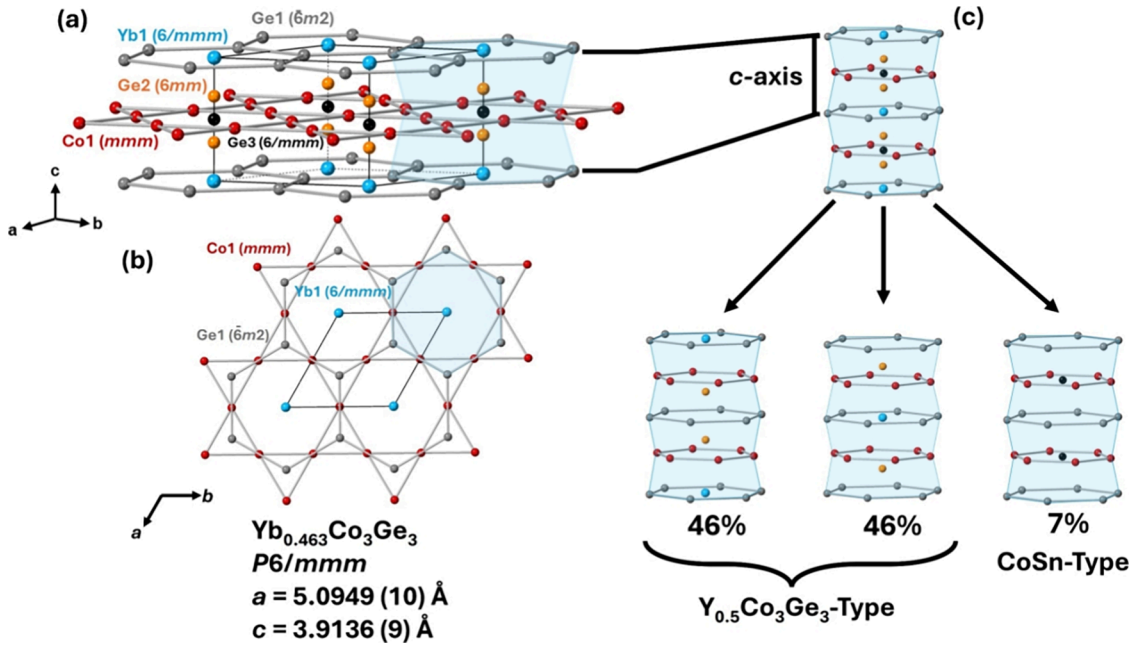

Figure 1. Previously reported structure of $Yb_{0.5}Co_3Ge_3$ with selected bonds omitted to emphasize the alternating stack of honeycomb nets and kagome nets along the *c*-axis.[18] (a) Full unit cell view. (b) View along the *c*-axis. (c) Structural motifs deconstructed with respective occupancies.

structural phase transitions seen in other kagome metals, with buckling of nets at low temperatures,[29] an in-plane twisting of the kagome lattice was discovered similar to what was reported with $MgCo_6Ge_6$.[30] The kagome distortion coincides with a kink in the resistivity observed around 95 K.[28] Additionally, anisotropic negative magnetoresistance was observed, further highlighting the anisotropy of this material. A related analog adopting the $HfFe_6Ge_6$ structure type, $YbFe_6Ge_6$ exhibits a magnetic spin reorientation at around 63 K, shifting the easy axis from *a* to *c*.[31] The $Y_{0.5}Co_3Ge_3$-type polymorph of $YbFe_6Ge_6$ does not display this reorientation and it is still unknown why this occurs.[32]

Herein, we report the single crystal growth and characterization of Fe-doped $Yb_{0.5}Co_3Ge_3$, as well as the change in magnetic and electrical properties with Fe substitution. In addition, the end members (x = 0.00 and 1.00) were also grown to compare the structural and physical property differences. The compounds were grown out of Sn flux and the structure and elemental compositions were determined using single crystal X-ray diffraction (SCXRD) and energy-dispersive (X-ray) spectroscopy (EDS). Increasing Fe substitution ($x \geq 0.50$) into the kagome sublattice results in structural order in the form similar to the $HfFe_6Ge_6$. Additionally, small amounts of Sn incorporation were detected from EDS. However, for simplicity, the nominal composition for all compounds will be referred to as $Yb_{0.5}(Co_{1-x}Fe_x)_3Ge_3$ (x = 0.00, 0.25, 0.50, 0.75, 1.00). Magnetic behavior is observed for all compositions as well as a change in the magnetic anisotropy as a function of x. Discussions regarding the advent of structural order are also included.

EXPERIMENTAL SECTION

Synthesis of $Yb_{0.5}(Co_{1-x}Fe_x)_3Ge_3$. Single crystals of $Yb_{0.5}(Co_{1-x}Fe_x)_3Ge_3$ (x = 0.00, 0.25, 0.50, 0.75, and 1.00) were grown using the flux growth method,[33] using Sn as the low-melting metal flux. The elements Yb:Co:Ge:Sn (Yb: 99.9% ingot, Co: 99.95% slug, Ge: 99.999% pieces, Sn: 99.99% shot in the ratio of 1.2:6 − x: 6:25) with an Fe concentration (Fe: 99.99% pieces) of x = 0.00, 1.50, 3.00, 4.50, and 6.00 were weighed out and placed into a Canfield alumina crucible set (2 mL container with 13 mm outer diameter)[34] with Sn flux above and below the other reactants to ensure homogeneity. The container was then sealed inside a fused silica tube under ~$^1/_3$ atm of Ar gas. These ampules were then heated in a programmable furnace from 300 to 1100 °C at a rate of 100 °C/h and dwelled at 1100 °C for 24 h. The sample containing ampules were then cooled to 900 °C at a rate of 1.5 °C/h. The samples dwelled for 72 h before they were then removed, inverted, and centrifuged to remove excess Sn flux. Excess flux present on the surface of the crystals was etched in 1:1 HCl/H_2O for 1 h. The product of the reaction yielded crystals of up to 4 mm with different morphologies ranging from needles to plates based on the amount of iron added.

The synthesis conditions described above are significantly different from the synthesis of the $Yb_{0.5}Co_3Ge_3$ that we initially reported[27] to optimize homogeneous Fe addition across the doped series. A 72 h dwell time was performed to ensure that samples were kept consistent between batches. The prevalence of the impurity, $Fe_{2-x}Ge$, increases as Fe-doping amounts increase. However, $Fe_{2-x}Ge$ was mechanically separable from the desired product.

Structure Determination. The crystal structures of $Yb_{0.5}(Co_{1-x}Fe_x)_3Ge_3$ (x = 0.00, 0.25, 0.50, 0.75, and 1.00) were determined using powder X-ray diffraction and single crystal X-ray diffraction (SCXRD). Powder X-ray diffraction data (Figures S1 and S2) were collected with a Bruker D2 Phaser (Cu Kα radiation, λ = 1.54184 Å). Single crystal data were collected using a Bruker D8 Quest Kappa single-crystal X-ray diffractometer with an IμS microfocus source (Mo Kα radiation, λ = 0.71073 Å) and a PHOTON III CPAD area detector. The raw data frames were integrated using the Bruker SAINT program, and a multiscan absorption correction was applied using SADABS.[35] Preliminary starting models were obtained with the intrinsic phasing method in SHELXT for compositions x = 0.00, 0.25, 0.75, and 1.00 and a direct method in SHELXS for x = 0.50 followed by refinement in SHELXL.[36] Crystallographic data and refinement parameters of each composition are listed in Table S1. Transition metal content was constrained to the values obtained from energy-dispersive spectroscopy.

Energy-dispersive (X-ray) spectroscopy (EDS) was performed on single crystals of $Yb_{0.5}(Co_{1-x}Fe_x)_3Ge_3$ (x = 0.00, 0.25, 0.50, 0.75, and 1.00) with a VERSA 3D focused ion beam scanning electron

https://doi.org/10.1021/acs.chemmater.5c00119
Chem. Mater. 2025, 37, 2302−2313

Table 1. Compositions of $Yb_{0.5}(Co_{1-x}Fe_x)_3Ge_3$* as Obtained from SCXRD and EDS Compared to the Nominal Composition

composition (x_{Fe})	SCXRD	SEM-EDS
Y-Type/CoSn-Type		
0.00	$Yb_{0.34}Co_3Ge_{2.78}Sn_{0.22}$	$Yb_{0.433(3)}Co_{3.000(2)}Ge_{2.513(2)}Sn_{0.268(5)}$
0.25	$Yb_{0.43}Co_{2.23}Fe_{0.77}Ge_{2.85}Sn_{0.15}$	$Yb_{0.448(2)}Co_{2.23(1)}Fe_{0.77(1)}Ge_{2.629(8)}Sn_{0.206(3)}$
H-Type		
0.50	$Yb_{0.90}Co_{3.17}Fe_{2.83}Ge_{5.80}Sn_{0.20}$	$Yb_{0.845(4)}Co_{3.16(4)}Fe_{2.83(4)}Ge_{5.25(3)}Sn_{0.54(2)}$
0.75	$Yb_{0.93}Co_{1.54}Fe_{4.46}Ge_{5.85}Sn_{0.15}$	$Yb_{0.888(2)}Co_{1.54(1)}Fe_{4.455(7)}Ge_{5.41(2)}Sn_{0.271(9)}$
1.00	$Yb_1Fe_6Ge_{5.82}Sn_{0.18}$	$Yb_{0.929(4)}Fe_{6.00(1)}Ge_{5.40(1)}Sn_{0.176(4)}$

*For x_{Fe} = 0.50, 0.75, and 1.00, the empirical formula was normalized to the "1-6-6" phase instead of the "0.5-3-3" phase.

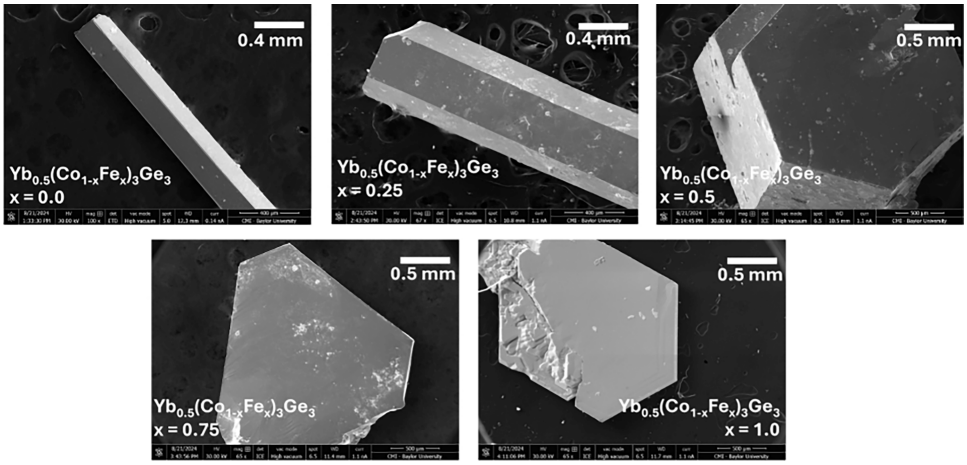

Figure 2. Images of single crystals of $Yb_{0.5}(Co_{1-x}Fe_x)_3Ge_3$ acquired from the SEM. Note the change in morphology from rods to plates with an increasing concentration of Fe.

microscope. An acceleration voltage of 20 kV and a spot size of 6.5 was used to collect data from five spots on each crystal. The compositions are given in Table 1 with a comparison to refined compositions obtained from SCXRD. Images of single crystals obtained from the SEM are shown in Figure 2; the crystal morphology changes from needles to plates as Fe is added. Tiny amounts of Sn are observed in the EDS data for these crystals that were grown out of Sn flux. The small amount is possibly from Sn substitution on Ge sites in the structure. We modeled for Sn in the most probable sites of incorporation across the doped series.[37,38]

Magnetic Properties. Measurements of temperature-dependent magnetic susceptibility (χ(T)) and isothermal field-dependent magnetization (M(H)) were obtained on single crystals using a VSM SQUID magnetometer from Quantum Design, Model MPMS-3. χ(T) was measured from 1.8 to 300 K under an applied field of H = 0.1 T parallel and perpendicular to the c-axis. The field-dependent measurements were taken at 1.8 K from −7 to 7 T parallel and perpendicular to the c-axis.

Resistivity. Temperature-dependent electrical resistivity (ρ(T)) was measured using a physical property measurement system (PPMS) from Quantum Design, model 6000 in the temperature range 1.8–300 K. Four Pt leads were mounted onto the polished single crystals by using silver paste. All samples had varying morphologies, thus the electrical current flowed parallel to the c-axis in x = 0.00 and 0.25 (rod-shaped crystals), and perpendicular to the c-axis in x = 0.50, 0.75, and 1.00 (plate-shaped crystals).

RESULTS

Crystal Structure. Figure 3 illustrates the relationship among the CoSn, $HfFe_6Ge_6$ (H-type), and $Y_{0.5}Co_3Ge_3$ (Y-type), structures. The H-type and Y-type structures are regarded as "stuffed variants" of the CoSn structure type.[39] Large electropositive elements insert in-plane into the center of the Ge1 hexagons of the honeycomb net and push out-of-plane

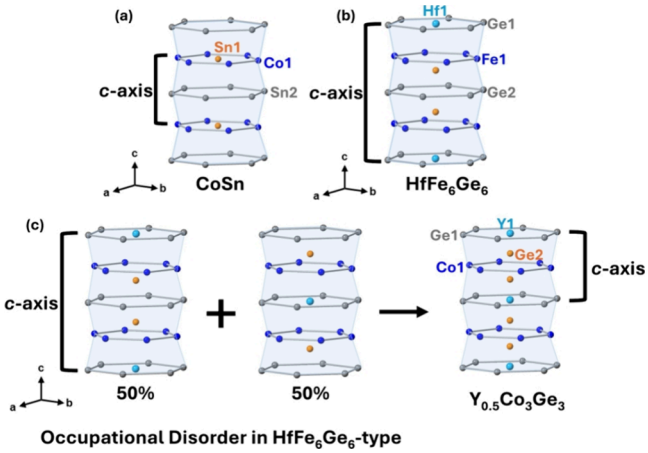

Figure 3. Staggered hexagonal channel motifs of the (a) CoSn, (b) $HfFe_6Ge_6$ (H-type), and (c) $Y_{0.5}Co_3Ge_3$ (Y-type) structure types, with selected bonds omitted. The relative c-axis length is emphasized in each of the structure types. (c) The $Y_{0.5}Co_3Ge_3$ structure type is made up of two H-type unit cells that are occupationally disordered with respect to one another.

the main group element initially centering the kagome net of the CoSn structure type through chemical pressure. All three structures consist of alternating (main group element) honeycomb and (transition metal) kagome slabs. The H-type structure represents the complete ordering of the electropositive and main group element dimers along the [001] direction. The random positional occupancy of the H-type structure averages 50% each, leading to the Y-type structure. This results in the reduction of the c-axis length of the unit cell

https://doi.org/10.1021/acs.chemmater.5c00119
Chem. Mater. 2025, 37, 2302−2313

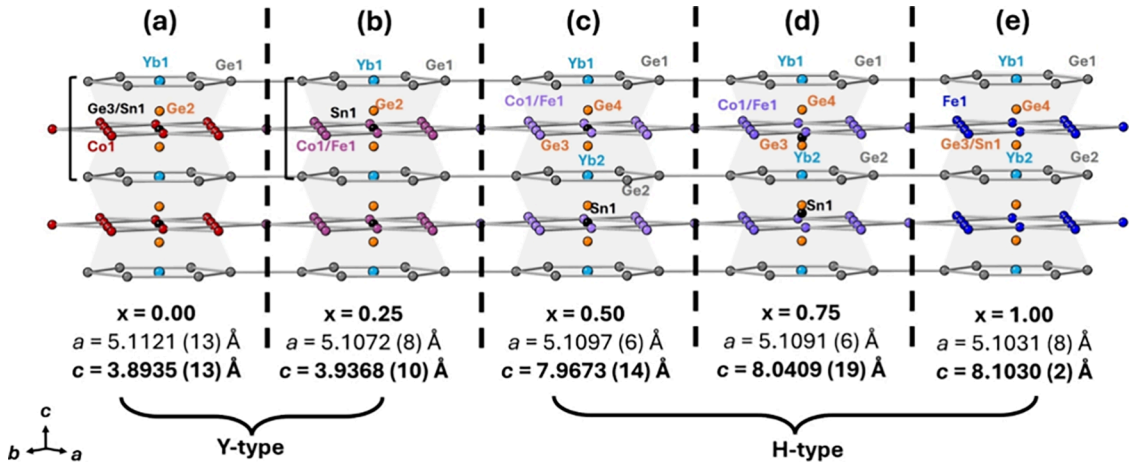

Figure 4. Crystal structures ((a) x = 0.00, (b) x = 0.25, (c) x = 0.50, (d) x = 0.75, and (e) x = 1.00) obtained from single crystal X-ray diffraction, highlighting only the staggered hexagonal channel. All structures have the same space group: *P6/mmm* and selected bonds are omitted. The brackets on the left of x = 0.00 and 0.25 indicate the c-axis length and the c-axis lengths beneath the structures are bolded. Structural information and representations are contained within the Supporting Information (Tables S1−S6 and Figures S3−S7).

by half and partial occupancy of the Y1 and Ge2 atoms. The Co end member of the $Yb_{0.5}(Co_{1-x}Fe_x)_3Ge_3$ series (x = 0.00) possesses a hybrid crystal structure of the Y-type and CoSn structure types,[27] while the Fe end member (x = 1.00) adopts the H-type.[22] As Fe is added in this hybrid system, the compositions x = 0.50 and 0.75 adopt a more ordered structure resembling the H-type variant. However, for simplicity, the formula $Yb_{0.5}(Co_{1-x}Fe_x)_3Ge_3$ will be used with x = 0.00, 0.25, 0.50, 0.75, 1.00 to describe each member of the doped series.

Figure 4 depicts the crystal structures of $Yb_{0.5}(Co_{1-x}Fe_x)_3Ge_3$. For simplicity, the staggered hexagonal channel is highlighted to compare how the site positions differ with the Fe addition. The nominal formula used in this article does not reflect the small amount of Sn substitution present; therefore, Table 1 provides the nominal concentrations compared to the formulas obtained from SCXRD and EDS. The complete structural information and representations are contained within the Supporting Information (Tables S1−S6 and Figures S3−S7). The partial occupancy of the atomic sites corresponds to the partial occupancy of the structural types present.

In x = 0.00 (Figure 4a), the hybrid $Y_{0.5}Co_3Ge_3$−CoSn structure type is present and the CoSn-type site is present with a higher probability than what was previously reported with nearly 31% occupancy. The differences in Yb occupancy are attributed to differences in synthesis conditions (reaction ratio of elements and temperature profile), the relative Yb content in this article is lower than what we previously reported.[27,28] Our report of $Gd_xCo_3(Ge, Sn)_3$ also had a reduced Gd occupancy and was grown from a Gd:Co:Ge:Sn 1−6−6−20 ratio.[37] We surmise that with increasing the relative Yb ratio in the growth, a corresponding increase in Yb occupancy will occur. x = 0.25 (Figure 4b) has a structure similar to that of x = 0.00, but the occupancy of the distinct structure types differs. The CoSn structure type is ∼15% in this case. As more Fe is added, the structure begins to deviate from the Y-type unit cell; the unit cell of x = 0.50 doubles along the c-axis, resembling the H-type structure. As shown in Figure 3, the $Y_{0.5}Co_3Ge_3$ (Y-type) structure can be described as disordered $HfFe_6Ge_6$ (H-type), exhibiting a 50% occupancy of the H-type positions. The x = 0.50 phase (Figure 4c) marks the first composition to display a difference in occupancy of this motif and thus causes the unit cell size to double. In addition, the 1*b* (6/*mmm*) Ge site (Ge3) present in x = 0.00, and 0.25 is displaced from the kagome plane in x = 0.50 (Sn1), resulting in its site symmetry being reduced (2*e*, 6*mm*). The x = 0.50 structure contains a rough model due to issues with indexing, which we analyze further in the Discussion section. The x = 0.75 phase (Figure 4d) also adopts a unit cell similar to the $HfFe_6Ge_6$-type and has differing occupancy of its motifs than x = 0.50. The Sn1 site still retains 6*mm* symmetry and exhibits a greater displacement from the kagome plane than x = 0.50. The x = 1.00 phase adopts the most ordered $HfFe_6Ge_6$-type cell when compared with the other compositions. There no longer exists an additional site that resembles the CoSn structure type, implying that the existence of Co influences the presence of a CoSn hybrid structure type.

A plot of cell dimensions as a function of Fe concentration is shown in Figure 5. The H-type structures (x = 0.50, 0.75, 1.00) were halved along the c-axis for easy comparison with the Y-type structures (x = 0.00, 0.25). As Fe is added, the c-axis length is increased while the a-axis length stays relatively constant.

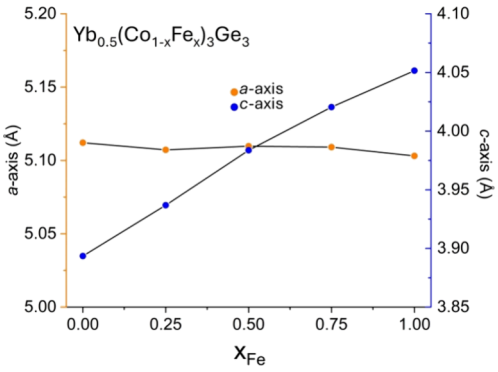

Figure 5. Cell dimensions as a function of Fe concentration in $Yb_{0.5}(Co_{1-x}Fe_x)_3Ge_3$ by using lattice constants from single crystal X-ray diffraction. The c-axis length was halved for x = 0.50, 0.75, and 1.00 for comparison across all compounds.

https://doi.org/10.1021/acs.chemmater.5c00119
Chem. Mater. 2025, 37, 2302−2313

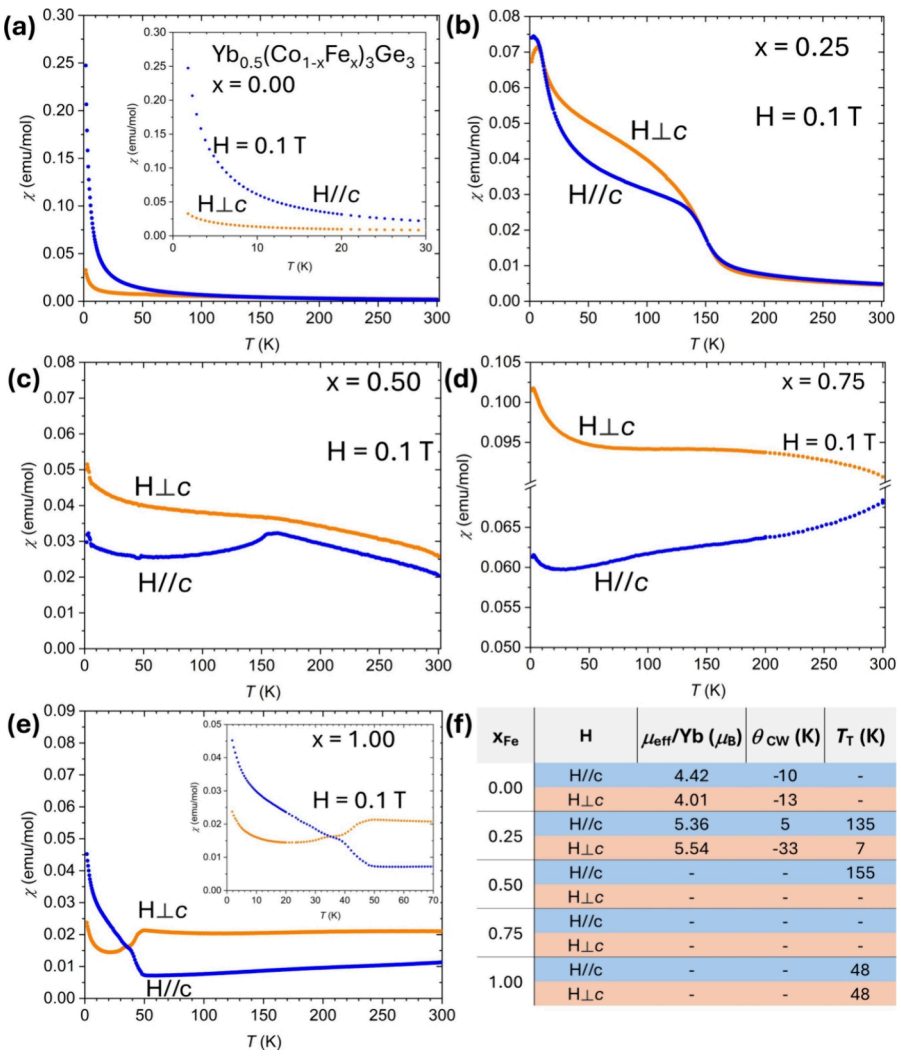

x_{Fe}	H	μ_{eff}/Yb (μ_B)	θ_{CW} (K)	T_T (K)
0.00	H//c	4.42	-10	-
	H⊥c	4.01	-13	-
0.25	H//c	5.36	5	135
	H⊥c	5.54	-33	7
0.50	H//c	-	-	155
	H⊥c	-	-	-
0.75	H//c	-	-	-
	H⊥c	-	-	-
1.00	H//c	-	-	48
	H⊥c	-	-	48

Figure 6. (a–e) Anisotropic temperature-dependent magnetometry measurements (H // c in blue and H ⊥ c in orange). Insets are magnifications of the low temperature data. (f) Observed magnetic moment per Yb (μ_{eff}/Yb), Curie–Weiss temperature (θ), and observed magnetic transition temperatures (T_T). Dashes indicate that values were unobtainable or no transitions were present in the data.

Magnetic Properties. To evaluate how the magnetic properties of $Yb_{0.5}(Co_{1-x}Fe_x)_3Ge_3$ change as a function of Fe addition, anisotropic temperature-dependent magnetic susceptibility measurements were performed, shown in Figure 6. The zero-field-cooled (ZFC) data set is reported here as there were no extreme differences between the ZFC and the field-cooled (FC) data. The isothermal field-dependent magnetization of each composition is given in Figure 7. Corresponding Curie–Weiss fits are given in the Supporting Information (Figures S8 and S9).

x = 0.00. The Co endmember in this series has been previously reported to have paramagnetic behavior with an effective magnetic moment of 4.23 μ_B,[27] lower than the calculated Yb^{3+} moment of μ_{eff} = 4.54 μ_B. In this work, the effective magnetic moment obtained from the Curie–Weiss fit of H // c is 4.42 μ_B, and that of H ⊥ c is 4.01 μ_B, and the Weiss constants are −10 and −13 K, respectively. The respective values agree with previous reports, and the moment obtained from the H ⊥ c data is reduced. The isothermal magnetization begins to saturate around 0.7 μ_B, which is similar in magnitude to what we previously reported (~1 μ_B).[27] It is possible that the reduction of Yb occupancy in the present compound is a determining factor in the field-dependent magnetization.

x = 0.25. The effective magnetic moments obtained from Curie–Weiss fits from 250 to 300 K are 5.36 and 5.54 μ_B for H // c and H ⊥ c, respectively. The elevated magnetic moment coupled with the ferromagnetic-like transition ~135 K of the H // c data indicates that as Fe is added into the kagome net, it begins to interact between slabs along the c-axis, and slight magnetic ordering is observed. The true magnetic moment of the Fe present could not be determined, as a rough Curie–Weiss fit was used. There also exists a Néel temperature at around 7 K in the H ⊥ c data. The isothermal magnetization shows a decrease in the magnitude of the H // c data compared to the x = 0.00 composition but still shows that the c-axis remains the easy axis with increasing field strength.

x = 0.50. A Néel temperature around 155 K is present, near where the Curie-like transition existed in x = 0.25. In addition, the H ⊥ c data have an increased magnitude of magnetization with no clear magnetic phase transitions. The isothermal magnetization shows slight hysteresis in both H ⊥ c, and H // c, while no hysteresis is observed in any of the other doped concentrations. Additionally, the H ⊥ c data show a higher magnetization with increasing field strength.

x = 0.75. No magnetic transitions are observed from 2 to 300 K; however, there is an enhanced magnitude of

https://doi.org/10.1021/acs.chemmater.5c00119
Chem. Mater. 2025, 37, 2302–2313

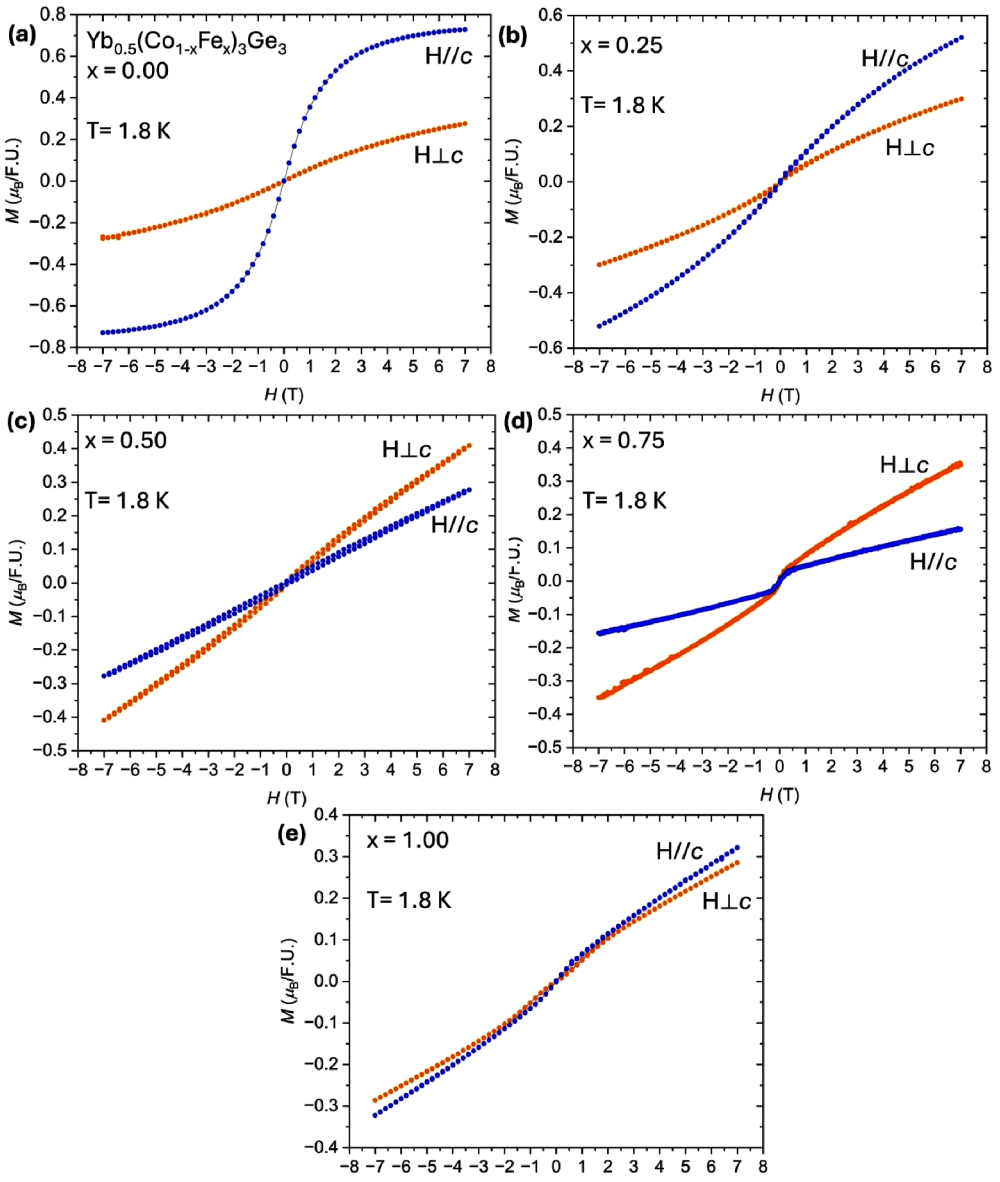

Figure 7. (a–e) Isothermal field-dependent magnetization of $Yb_{0.5}(Co_{1-x}Fe_x)_3Ge_3$ (x = 0.00, 0.25, 0.50, 0.75, and 1.00) measured at 1.8 K.

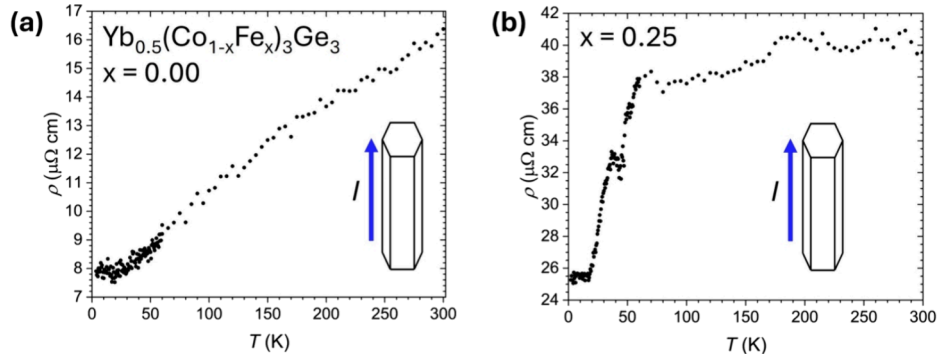

Figure 8. (a, b) Temperature dependent resistivity, ρ, of x = 0.00 and 0.25. The hexagonal 3D shapes represent the morphology of the samples, with the blue arrow representing the direction of the applied current. For (a) and (b), this is parallel to the c-axis.

magnetization of the H⊥c compared to H//c. In addition, there is an upturn in the H//c data near 300 K. In the isothermal magnetization, the difference in magnitude of the H // c and H ⊥ c data is much larger than x = 0.50.

x = 1.00. The Fe end member of the series displays similar behavior to what was previously reported by Avila et al.[31] In the previous report, a spin reorientation at 63 K was observed, resulting in easy-axis inversion from the *ab* plane to the *c*-axis, and could not be detected in the polycrystalline measurements.

https://doi.org/10.1021/acs.chemmater.5c00119
Chem. Mater. 2025, 37, 2302−2313

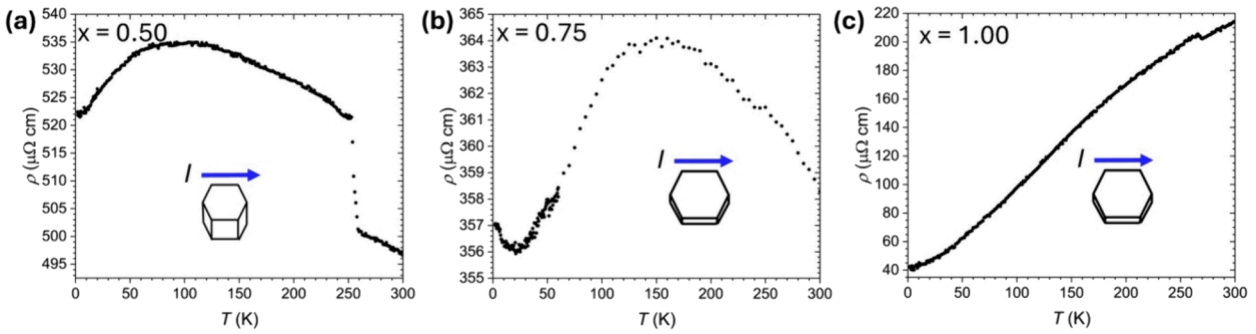

Figure 9. (a–c) Temperature-dependent resistivity, ρ, of x = 0.50, 0.75, and 1.00. The hexagonal 3D shapes represent the morphology of the samples with the blue arrow representing the direction of the applied current. For (a–c), the current is applied parallel to the *ab* plane.

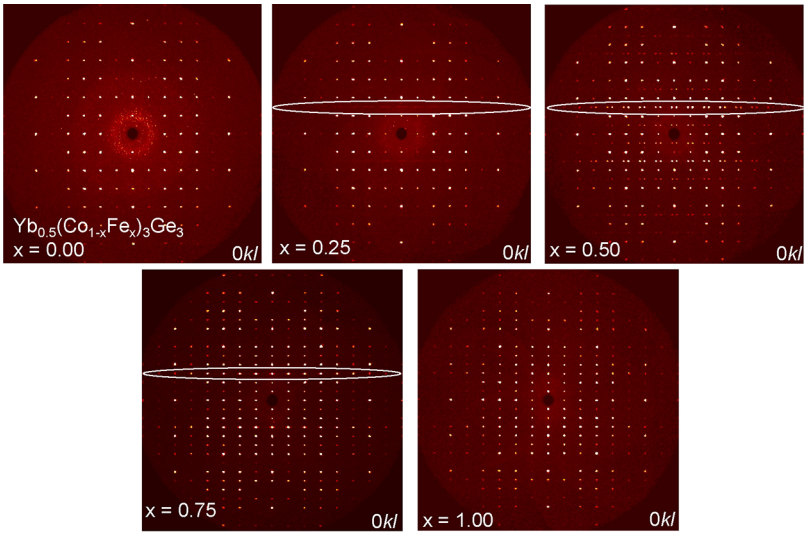

Figure 10. (a) 0*kl* diffraction patterns for $Yb_{0.5}(Co_{1-x}Fe_x)_3Ge_3$ (x = 0.00, 0.25, 0.50, 0.75, and 1.00) obtained from single crystal X-ray diffraction data. A circled area is shown on x = 0.00, 0.25, 0.50, 0.75, and 1.00 on the (0*k*1.5) set of planes for x = 0.00, 0.25, and (0*k*3) set of planes for x = 0.50, 0.75, and 1.00 to emphasize either the diffuse scattering or the broad satellite peaks.

Here, the spin reorientation is observed at ∼50 K with the same anisotropy. Additionally, the temperature-dependent magnetization below the spin reorientation seems to increase drastically in H // *c* instead of the saturation previously observed. The isothermal magnetization shows similar magnitudes along both directions at 1.8 K.

Resistivity. The resistivity, ρ, for the Co end member, x = 0.00, as a function of T decreases linearly down to low temperatures with no observed transition exhibiting simple metallic behavior (Figure 8a) in agreement with previous reports.[27] The slight increase in the resistivity at 5 K and the kink at 95 K of previously reported $Yb_{0.5}Co_3Ge_3$ is not seen here and likely originates from the different amounts of occupational disorder or hybridization of the two structure types ($Y_{0.5}Co_3Ge_3$ and CoSn).[27,28] Least-squares fitting of resistivity with $\rho - \rho_0 \propto T^n$ in 3.5 K < T < 40 K gave n = 3.6 ± 1.1, and fitting of up to 50 K gave n = 2.4 ± 0.4.[40] These n values suggest that other scattering mechanisms besides noninteracting electron–electron scattering (n = 2) are present, such as electron–phonon scattering and electron-impurity scattering.[41] Electron-magnetic impurity (Kondo) scattering and weak localization effects have been proposed to influence the low-temperature resistivity data, but neither has been ruled out. Due to the intrinsic amount of structural disorder, the values of n have relatively large errors, but the trend of increasing n with lower temperature ranges persists. In x = 0.25, the resistivity drastically drops at ∼60 K (Figure 8b), followed by another anomaly at ∼45 K after which it smooths at 17 K. Satisfactory fits of $\rho - \rho_0 \propto T^n$ could not be obtained for x = 0.25.

Starting with x = 0.50, in Figure 9a–c, the crystal morphology switches from rod-shaped to plate-shaped, which coincides with a change in the direction of the applied current (from parallel to *c*-axis to parallel to the *ab* plane). For x = 0.50, there is a drastic increase in the resistivity of around 259 K (Figure 9a) with a broad maximum at ∼100 K.[42] The resistivity for x = 0.75 (Figure 9b) shows a broad maximum at ∼150 K, then drops sharply below this temperature, and begins to saturate as the temperature decreases. The resistivity of the Fe-end member, x = 1.00, (Figure 9c) is in general agreement with previous reports, albeit the high-temperature anomaly reported herein at ∼250 K was previously not observed.[31] Power-law fits ranging from 2 to 30, 40, and 50 K gave values of n = 1.4 ± 0.2, 1.5 ± 0.1, and 1.6 ± 0.07, respectively. This agrees with a decrease in electron–phonon scattering, as lower temperature ranges are fit. While x = 0.00, 0.25, 0.75, and 1.00 all see an overall decrease in resistivity as temperature decreases, for x = 0.50, there is a net increase.

https://doi.org/10.1021/acs.chemmater.5c00119
Chem. Mater. 2025, 37, 2302–2313

DISCUSSION

Structural Evolution. When viewing the 0*kl* direction of the diffraction pattern for $Yb_{0.5}(Co_{1-x}Fe_x)_3Ge_3$ (x = 0.00, 0.25, 0.50, 0.75, 1.00), either diffuse scattering or broad satellite peaks can be seen in most of the doped compositions (x = 0.25, 0.50, 0.75), shown in Figures 10 and 11a. When

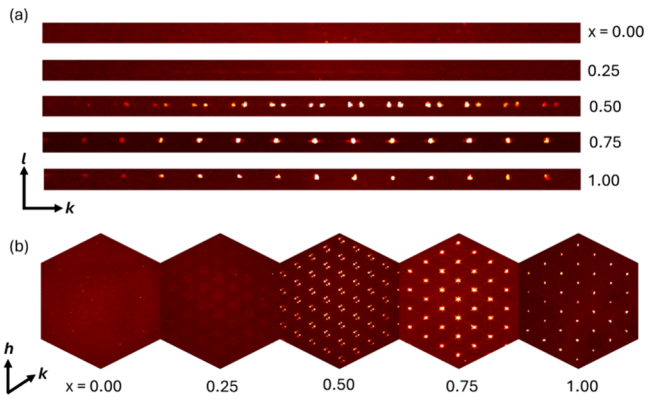

Figure 11. (a) Zoomed-in view of the 0*k*1.5 set of planes (x = 0.00, 0.25) and on the 0*k*3 set of planes (x = 0.50, 0.75, 1.00). (b) Section of the *hk*1.5 and *hk*3 views of the reciprocal lattice.

examining the *hk*1.5 (x = 0.00, 0.25) and *hk*3 (x = 0.50, 0.75, and 1.00) sections of the reciprocal lattice, the diffuse scattering converges into one reflection as the Fe content increases as shown in Figure 11b. Diffuse scattering in the AM_6X_6 family has been observed before with M = Co.[43] Diffuse scattering occurs when X-rays interact with a material that has disorder or irregularity in its crystal structure. Unlike Bragg scattering, which results in sharp, well-defined peaks corresponding to the average periodic structure of a crystal, diffuse scattering appears as a spread-out signal over a range of angles and will require pair distribution function analysis (PDF) and the usage of synchrotron sources to probe local structure.[44−46] The extra reflections in x = 0.50 indicate that a larger unit cell or the addition of incommensurate modulation vectors is needed, as they are not indexed when using the current hexagonal unit cell. Unsuccessful attempts to model this composition with an orthorhombic cell were made to index the reflections as twin domains. Figures S10 and S11 show the indexed reflections of x = 0.50 using both the hexagonal and orthorhombic cells, respectively. Regarding the *hk*3 precession image in Figure 11b for x = 0.50, there are clear complex diffraction features that are not uncommon in AFe_6Sn_6 compounds, which may be due to a "twinned microstructure".[47,48] We speculate the diffuse scattering observed as well as the unindexable extra reflections present in x = 0.50 are caused by incommensurate ordering intrinsic to the crystal structure. Although the *hk*3 reflections were focused on for this x = 0.50 discussion, the extra reflections are present on other l = odd precession planes, except for *hk*7.

The polymorphism and superstructure ordering in the AM_6X_6 family were detailed by Fredrickson et al.[49] It was found that $ScFe_6Ge_6$ with the hexagonal $HfFe_6Ge_6$ structure type (space group: *P*6/*mmm*) is dominated by electrostatic effects while $ScFe_6Ga_6$ with the orthorhombic $ScFe_6Ga_6$ structure type (space group: *Immm*) is primarily influenced by unfavorable steric interactions. It is the competition of these two effects that leads to the structural variety in this family. The $Y_{0.5}Co_3Ge_3$ structure type is an outlier in this family that maintains its hexagonal symmetry while bypassing the steric obstacles of the large electropositive element. This specific polymorphism between orthorhombic superstructures and the Y-type is seen with AFe_6Ge_6, with A being the larger lanthanides.[50] The isolation of either phase was observed to be dependent on synthesis conditions. With this in mind, specific interatomic distances were analyzed across this doped series. As Fe content increases, the M1−M1 interatomic distances that encompass the local environment of the Yb increase, as shown in Figure 12. The $M1-M1_{c\text{-axis}}$ distances change significantly relative to the $M1-M1_{ab\ plane}$ distances, showing a similar trend as the lattice parameters in Figure 5. The 20-coordinate environment that surrounds Yb becomes larger as more Fe is added, allowing for a sterically favored configuration, leading to the structural order that arises. The majority of studies of structural transitions from the H-type to other orthorhombic variants in AM_6X_6 vary the X element composition through substitution.[39,49,51,52] One example of structural deviation with varied transition metal contents is in $YbMn_{6-x}Fe_xSn_6$. The $YbMn_6Sn_6$ parent compound hosts an intermediate valent Yb state and adopts a slightly disordered H-type structure.[53,54] As Fe is added into the Mn sublattice, the chemical pressure surrounding the Yb atom causes the structure to shift to the $HoFe_6Sn_6$-type, an orthorhombic structure type with space group *Immm*.[53,54] A summary of this concept is shown in Figure S12. As the chemical pressure increases around the A site, the A elements form a staggered configuration with respect to one another along their respective axes. The frequency of this staggering decreases from the $ErFe_6Sn_6$-type, with every four A sites, to the $ScFe_6Ga_6$ structure, type, the most sterically favored configuration with every other A element being staggered. The

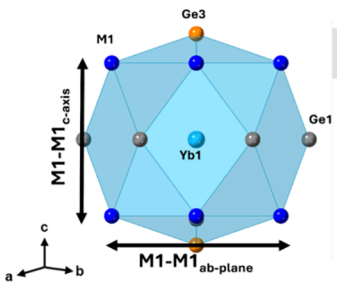

$Yb_{0.5}(Co_{1-x}Fe_x)_3Ge_3$

x_{Fe}	$M1-M1_{c\text{-axis}}$ (Å)	$M1-M1_{ab\text{-plane}}$ (Å)
0.00	3.8935 (13)	4.4272 (11)
0.25	3.9368 (10)	4.4230 (7)
0.50	3.9836 (7)	4.4251 (5)
0.75	4.0204 (10)	4.4246 (5)
1.00	4.0514 (11)	4.4194 (7)

Figure 12. Local environment of Yb1 with the M1−M1 (M= Co, Fe) interatomic distances emphasized. The M1−M1 distance along the *c*-axis increases as Fe is incorporated, while the M1−M1 distance along the *ab* plane remains relatively constant. This increase in the $M1-M1_{c\text{-axis}}$ causes the interstitial space that the Yb occupies to increase.

https://doi.org/10.1021/acs.chemmater.5c00119
Chem. Mater. 2025, 37, 2302−2313

$Y_{0.5}Co_3Ge_3$ structure type is shown as an alternative way to crystallize, showing a random ordering of the A element. The complex ordering of the "166" phases is a possible reason why the morphology of the disordered members of the $Yb_{0.5}(Co_{1-x}Fe_x)_3Ge_3$ series (x = 0.00, 0.25) form hexagonal needles, while the ordered members (x = 0.75 and 1.00) form hexagonal plates. x = 0.50 has a hexagonal block shape, which is an intermediate morphology of the needles and plates. The ordering of the A element is greatly affected along the same axes that the alternating layers run parallel to (ab plane in the hexagonal H-type structure) in the polymorphs of this structure. It is plausible that crystallization along the ab plane is less favorable, resulting in needles for the randomly disordered structures (Y-type) and more plate-like for the ordered structures (H-type).

Physical Properties. Within the temperature-dependent magnetic data taken from 1.8 to 300 K, magnetic transitions are present only in x = 0.25, 0.50, and 1.00. Previously reported ACo_6Ge_6 (A = Y, Dy, Er−Lu) compounds show paramagnetic behavior from 78 to 293 K and no Co magnetic contribution in the temperature-dependent magnetic susceptibility.[55] Our prior report of $Gd_xCo_3(Ge,Sn)_3$ did display Co contribution in the temperature-dependent magnetic data with H // a.[37] Fe moments within the pure AFe_6Ge_6 (A = Sc, Y, Nd, Sm, and Gd−Lu) have shown to independently and antiferromagnetically order at temperatures ranging from 400 to 500 K.[22,56] The Yb analog is the only one that has shown this drastic spin reorientation of the Fe sublattice at low temperatures and also only occurs in the ordered H-type polymorph.[32] Through neutron diffraction studies, the Fe sublattice was determined to order ferromagnetically with antiferromagnetic order between neighboring Fe slabs in an axial configuration along the c-axis.[57−59] We hypothesize that as Fe is substituted for Co in $Yb_{0.5}Co_3Ge_3$, long-range magnetic ordering is introduced between the kagome layers in an axial fashion along the c-axis. In x = 0.25, the Fe content is insufficient, causing a low-temperature ferromagnetic-like transition at ∼135 K as well as a low-temperature Néel transition (T_N) at 7 K in H ⊥ c. The T_N in the H ⊥ c data is reminiscent of planar antiferromagnetic ordering akin to the behavior in FeSn.[60] As more Fe is added, in x = 0.50, a clear T_N is observed at 155 K. The field-dependent data support how Fe introduces long-range ordering in this system by showing the change in anisotropy. Increasing the Fe content promotes interlayer antiferromagnetic ordering along the c-axis thus causing the easy axis to invert. The data was collected at 1.8 K, which explains why the trend breaks at x = 1.00, as the pure Fe endmember undergoes a spontaneous change in anisotropy at 48 K, which is unaffected by the strength of the applied field up to 7 T.

The change in magnitudes of the resistivity (Figures 8 and 9) for each compound is in line with the intrinsic disorder visible in single-crystal X-ray structural models. The residual resistivities (ρ_0) for x = 0.00, 0.25, 0.50, 0.75, and 1.00 are 8, 25, 522, 357, and 42 μΩ cm, respectively. High ρ_0 values usually correspond to high degrees of structural disorder. Here, we have compounds subjected to not only structural disorder but also compositional disorder. For x = 0.00 and 0.25, the resistivity was measured along the c-axis or along the length of the needle-shaped crystal, but for x = 0.50, 0.75, and 1.00, the resistivity was measured parallel to the ab plane or perpendicular to the thickness of the plate-shaped crystal due to the change in morphology. The lack of direct trends as Co is substituted for Fe could be due, in part, to the fact that the electrical transport for x = 0.00 and 0.25 is measured perpendicular to the alternating hexagonal and kagome slabs, but for x = 0.50, 0.75, and 1.00, the electrical transport is measured parallel to the slabs. We speculate that this results in a change of observable electron scattering as temperature is decreased.

CONCLUSIONS

In this article, we report the single crystal growth and X-ray diffraction of $Yb_{0.5}(Co_{1-x}Fe_x)_3Ge_3$ (x = 0.00, 0.25, 0.50, 0.75, and 1.00). The substitution of Fe results in a larger local environment around the Yb atoms, subsequently leading to the ordered $HfFe_6Ge_6$-type structure that arises. The diffuse scattering in x = 0.25, 0.50, and 0.75 points to the possibility that the local symmetry is being altered, which has been observed in the closely related $(Co_{0.45}Fe_{0.55})Sn$.[61] Endeavors in probing the local environments of this material will give way to understanding how the change in structure relates to the change in the physical properties. The magnetic interactions of the $Yb_{0.5}(Co_{1-x}Fe_x)_3Ge_3$ doped series appear to predominately occur along the c-axis suggesting that the moments are coupled with one another between the layers. Obtaining the magnetic structures of these compounds is an avenue for future studies. A study recently reported by the Shatruk group explored the characteristics of polycrystalline $YFe_{6-x}Co_6Ge_6$.[62] A similar trend is observed in the magnetic susceptibility, with the T_N suppressing to lower temperatures with reduced Fe content. Additionally, the density-functional theory (DFT) calculations reveal that the increasing Co content leads to the filling of 3d states, moving the density of states (DOS) further away from the Fermi level, which rationalized the ferromagnetic-like behavior observed.

According to the least-squares fitting of the experimental resistivity data with $\rho - \rho_0 \propto T^n$ for $Yb_{0.5}(Co_{1-x}Fe_x)_3Ge_3$, we suspect the interplay of multiple scattering mechanisms and crystal electric field effects for all members of this series. It is clear that as Co becomes increasingly substituted for Fe, the electronic structures of these Kagome materials are drastically changing, providing a rich platform to study strong correlations. Band structure calculations and field-dependent and pressure-dependent resistivity measurements will help unravel the dominant scattering mechanisms that give rise to the seemingly complex electronic structures presented here.

ASSOCIATED CONTENT

Supporting Information

The Supporting Information is available free of charge at https://pubs.acs.org/doi/10.1021/acs.chemmater.5c00119.

(Figures S1 and S2) Powder diffraction patterns of $Yb_{0.5}(Co_{1-x}Fe_x)_3Ge_3$ (x = 0.00, 0.25, 0.50, 0.75, and 1.00); (Table S1) crystallographic data and refinement parameters; (Figures S3−S7) full unit cells of $Yb_{0.5}(Co_{1-x}Fe_x)_3Ge_3$ (x = 0.00, 0.25, 0.50, 0.75, and 1.00); (Tables S2−S6) atomic coordinates and atomic displacement parameters; (Figures S8 and S9) Curie−Weiss fitted data for $Yb_{0.5}(Co_{1-x}Fe_x)_3Ge_3$ (x = 0.00 and 0.25); (Figures S10 and S11) indexed precession images of $Yb_{0.5}(Co_{1-x}Fe_x)_3Ge_3$ (x = 0.50) to highlight the extra reflections; (Figure S12) structural comparison of the "166" phases (PDF)

https://doi.org/10.1021/acs.chemmater.5c00119
Chem. Mater. 2025, 37, 2302−2313

Accession Codes

CCDC 2417068 ($Yb_{0.34}Co_3Ge_{2.78}Sn_{0.22}$), CCDC 2417069 ($Yb_{0.43}Co_{2.23}Fe_{0.77}Ge_{2.85}Sn_{0.15}$), CCDC 2417071 ($Yb_{0.93}Co_{1.54}Fe_{4.46}Ge_{5.85}Sn_{0.15}$), and CCDC 2417079 ($YbFe_6Ge_{5.82}Sn_{0.18}$) contain the supplementary crystallographic data for this paper. These data can be obtained free of charge via www.ccdc.cam.ac.uk/data_request/cif, or by emailing data_request@ccdc.cam.ac.uk, or by contacting The Cambridge Crystallographic Data Centre, 12 Union Road, Cambridge CB2 1EZ, UK; fax: + 44 1223 336033.

AUTHOR INFORMATION

Corresponding Author

Julia Y. Chan − *Department of Chemistry and Biochemistry, Baylor University, Waco, Texas 76706, United States;* orcid.org/0000-0003-4434-2160; Email: Julia_Chan@baylor.edu

Authors

Rahul Meduri − *Department of Chemistry and Biochemistry, Baylor University, Waco, Texas 76706, United States*

Mario A. Plata − *Department of Chemistry and Biochemistry, Baylor University, Waco, Texas 76706, United States*

Gregory T. McCandless − *Department of Chemistry and Biochemistry, Baylor University, Waco, Texas 76706, United States*

Benny C. Schundelmier − *Department of Physics, Florida State University, Tallahassee, Florida 32306, United States; National High Magnetic Field Laboratory, Florida State University, Tallahassee, Florida 32310, United States;* orcid.org/0000-0002-7345-9977

Mehak Ghafoor − *Department of Physics, Florida State University, Tallahassee, Florida 32306, United States; National High Magnetic Field Laboratory, Florida State University, Tallahassee, Florida 32310, United States*

Kaya Wei − *National High Magnetic Field Laboratory, Florida State University, Tallahassee, Florida 32310, United States*

Complete contact information is available at: https://pubs.acs.org/10.1021/acs.chemmater.5c00119

Notes

The authors declare no competing financial interest.

ACKNOWLEDGMENTS

J.Y.C. and R.M. acknowledge DOE: DE-SC0022854 and Welch: AA-2056-20240404 for support of this work. A portion of this work was performed at the National High Magnetic Field Laboratory (NHMFL), which is supported by National Science Foundation Cooperative Agreement No. DMR-2128556 and the State of Florida. B.S., M.G., and K.W. acknowledge the support of the NHMFL User Collaboration Grant Program (UCGP).

REFERENCES

(1) Wang, Y.; Wu, H.; McCandless, G. T.; Chan, J. Y.; Ali, M. N. Quantum States and Intertwining Phases in Kagome Materials. *Nat. Rev. Phys.* **2023**, *5*, 635−658.

(2) Jovanovic, M.; Schoop, L. M. Simple Chemical Rules for Predicting Band Structures of Kagome Materials. *J. Am. Chem. Soc.* **2022**, *144*, 10978−10991.

(3) Ortiz, B. R.; Gomes, L. C.; Morey, J. R.; Winiarski, M.; Bordelon, M.; Mangum, J. S.; Oswald, I. W. H.; Rodriguez-Rivera, J. A.; Neilson, J. R.; Wilson, S. D.; Ertekin, E.; McQueen, T. M.; Toberer, E. S. New Kagome Prototype Materials: Discovery of KV_3Sb_5, RbV_3Sb_5, and CsV_3Sb_5. *Phys. Rev. Mater.* **2019**, *3*, No. 094407.

(4) Li, H.; Zhang, T. T.; Yilmaz, T.; Pai, Y. Y.; Marvinney, C. E.; Said, A.; Yin, Q. W.; Gong, C. S.; Tu, Z. J.; Vescovo, E.; Nelson, C. S.; Moore, R. G.; Murakami, S.; Lei, H. C.; Lee, H. N.; Lawrie, B. J.; Miao, H. Observation of Unconventional Charge Density Wave without Acoustic Phonon Anomaly in Kagome Superconductors AV_3Sb_5 (A = Rb, Cs). *Phys. Rev. X* **2021**, *11*, No. 031050.

(5) Ortiz, B. R.; Teicher, S. M. L.; Hu, Y.; Zuo, J. L.; Sarte, P. M.; Schueller, E. C.; Abeykoon, A. M. M.; Krogstad, M. J.; Rosenkranz, S.; Osborn, R.; Seshadri, R.; Balents, L.; He, J.; Wilson, S. D. CsV_3Sb_5: A Z_2 Topological Kagome Metal with a Superconducting Ground State. *Phys. Rev. Lett.* **2020**, *125*, No. 247002.

(6) Yang, S.-Y.; Wang, Y.; Ortiz, B. R.; Liu, D.; Gayles, J.; Derunova, E.; Gonzalez-Hernandez, R.; Šmejkal, L.; Chen, Y.; Parkin, S. S. P.; Wilson, S. D.; Toberer, E. S.; McQueen, T.; Ali, M. N. Giant, Unconventional Anomalous Hall Effect in the Metallic Frustrated Magnet Candidate, KV_3Sb_5. *Sci. Adv.* **2020**, *6*, No. eabb6003.

(7) Yu, F. H.; Wu, T.; Wang, Z. Y.; Lei, B.; Zhuo, W. Z.; Ying, J. J.; Chen, X. H. Concurrence of Anomalous Hall Effect and Charge Density Wave in a Superconducting Topological Kagome Metal. *Phys. Rev. B* **2021**, *104*, No. L041103.

(8) Ortiz, B. R.; Teicher, S. M. L.; Kautzsch, L.; Sarte, P. M.; Ratcliff, N.; Harter, J.; Ruff, J. P. C.; Seshadri, R.; Wilson, S. D. Fermi Surface Mapping and the Nature of Charge-Density-Wave Order in the Kagome Superconductor CsV_3Sb_5. *Phys. Rev. X* **2021**, *11*, No. 041030.

(9) Kautzsch, L.; Ortiz, B. R.; Mallayya, K.; Plumb, J.; Pokharel, G.; Ruff, J. P. C.; Islam, Z.; Kim, E.-A.; Seshadri, R.; Wilson, S. D. Structural Evolution of the Kagome Superconductors AV_3Sb_5 (A = K, Rb, and Cs) Through Charge Density Wave Order. *Phys. Rev. Mater.* **2023**, *7*, No. 024806.

(10) Teng, X.; Chen, L.; Ye, F.; Rosenberg, E.; Liu, Z.; Yin, J.-X.; Jiang, Y.-X.; Oh, J. S.; Hasan, M. Z.; Neubauer, K. J.; Gao, B.; Xie, Y.; Hashimoto, M.; Lu, D.; Jozwiak, C.; Bostwick, A.; Rotenberg, E.; Birgeneau, R. J.; Chu, J.-H.; Yi, M.; Dai, P. Discovery of Charge Density Wave in a Kagome Lattice Antiferromagnet. *Nature* **2022**, *609*, 490−495.

(11) Shao, S.; Yin, J.-X.; Belopolski, I.; You, J.-Y.; Hou, T.; Chen, H.; Jiang, Y.; Hossain, M. S.; Yahyavi, M.; Hsu, C.-H.; Feng, Y. P.; Bansil, A.; Hasan, M. Z.; Chang, G. Intertwining of Magnetism and Charge Ordering in Kagome FeGe. *ACS Nano* **2023**, *17*, 10164−10171.

(12) Wu, X.; Mi, X.; Zhang, L.; Wang, C.-W.; Maraytta, N.; Zhou, X.; He, M.; Merz, M.; Chai, Y.; Wang, A. Annealing-Tunable Charge Density Wave in the Magnetic Kagome Material FeGe. *Phys. Rev. Lett.* **2024**, *132*, No. 256501.

(13) Hou, Z.; Ren, W.; Ding, B.; Xu, G.; Wang, Y.; Yang, B.; Zhang, Q.; Zhang, Y.; Liu, E.; Xu, F.; Wang, W.; Wu, G.; Zhang, X.; Shen, B.; Zhang, Z. Observation of Various and Spontaneous Magnetic Skyrmionic Bubbles at Room Temperature in a Frustrated Kagome Magnet with Uniaxial Magnetic Anisotropy. *Adv. Mater.* **2017**, *29*, No. 1701144.

(14) Kida, T.; Fenner, L. A.; Dee, A. A.; Terasaki, I.; Hagiwara, M.; Wills, A. S. The Giant Anomalous Hall Effect in the Ferromagnet Fe_3Sn_2−a Frustrated Kagome Metal. *J. Phys.: Condens. Matter* **2011**, *23*, No. 112205.

(15) Natarajan, S.; Rao, G. V. S.; Baskaran, R.; Radhakrishnan, T. S. Synthesis and Electrical Properties of Shandite-Parkerite Phases, $A_2M_3Ch_2$. *J. Less-Common Met.* **1988**, *138*, 215−224.

(16) Vaqueiro, P.; Sobany, G. G. A Powder Neutron Diffraction Study of the Metallic Ferromagnet $Co_3Sn_2S_2$. *Solid. State. Sci.* **2009**, *11*, 513−518.

(17) Wang, Q.; Xu, Y.; Lou, R.; Liu, Z.; Li, M.; Huang, Y.; Shen, D.; Weng, H.; Wang, S.; Lei, H. Large Intrinsic Anomalous Hall Effect in Half-Metallic Ferromagnet $Co_3Sn_2S_2$ with Magnetic Weyl Fermions. *Nat. Commun.* **2018**, *9*, 3681.

(18) Xu, X.; Yin, J.-X.; Qu, Z.; Jia, S. Quantum Interactions in Topological R166 Kagome Magnet. *Rep. Prog. Phys.* **2023**, *86*, No. 114502.

(19) Arachchige, H. W. S.; Meier, W. R.; Marshall, M.; Matsuoka, T.; Xue, R.; McGuire, M. A.; Hermann, R. P.; Cao, H.; Mandrus, D. Charge Density Wave in Kagome Lattice Intermetallic ScV_6Sn_6. *Phys. Rev. Lett.* **2022**, *129*, No. 216402.
(20) Ortiz, B. R.; Meier, W. R.; Pokharel, G.; Chamorro, J.; Yang, F.; Mozaffari, S.; Thaler, A.; Gomez Alvarado, S. J.; Zhang, H.; Parker, D. S.; Samolyuk, G. D.; Paddison, J. A. M.; Yan, J.; Ye, F.; Sarker, S.; Wilson, S. D.; Miao, H.; Mandrus, D.; McGuire, M. A. Stability Frontiers in the AM_6X_6 Kagome Metals: The $LnNb_6Sn_6$ (Ln:Ce−Lu,Y) Family and Density-Wave Transition in $LuNb_6Sn_6$. *J. Am. Chem. Soc.* **2025**, *147*, 5279−5292.
(21) Meier, W. R.; Madhogaria, R. P.; Mozaffari, S.; Marshall, M.; Graf, D. E.; McGuire, M. A.; Arachchige, H. W. S.; Allen, C. L.; Driver, J.; Cao, H.; Mandrus, D. Tiny Sc Allows the Chains to Rattle: Impact of Lu and Y Doping on the Charge-Density Wave in ScV_6Sn_6. *J. Am. Chem. Soc.* **2023**, *145*, 20943−20950.
(22) Venturini, G.; Welter, R.; Malaman, B. Crystallographic Data and Magnetic Properties of RT_6Ge_6 compounds (R = Sc, Y, Nd, Sm, Gd-Lu; T = Mn, Fe). *J. Alloys Compd.* **1992**, *185*, 99−107.
(23) Malaman, B.; Venturini, G.; Roques, B. Nouveaux Stannures Ternaires: MMn_6Sn_6 (M = Sc, Y, Sm, Gd-Tm, Lu) ET $ScFe_6Sn_6$. *Mater. Res. Bull.* **1988**, *23*, 1629−1633.
(24) Clatterbuck, D. M.; Gschneidner, K. A. Magnetic Properties of RMn_6Sn_6 (R = Tb, Ho, Er, Tm, Lu) Single Crystals. *J. Magn. Magn. Mater.* **1999**, *207*, 78−94.
(25) Malaman, B.; Venturini, G.; Welter, R.; Sanchez, J. P.; Vulliet, P.; Ressouche, E. Magnetic Properties of RMn_6Sn_6 (R = Gd−Er) Compounds From Neutron Diffraction and Mössbauer Measurements. *J. Magn. Magn. Mater.* **1999**, *202*, 519−534.
(26) Ma, W.; Xu, X.; Yin, J.-X.; Yang, H.; Zhou, H.; Cheng, Z.-J.; Huang, Y.; Qu, Z.; Wang, F.; Hasan, M. Z.; Jia, S. Rare Earth Engineering in RMn_6Sn_6 (*R*=Gd-Tm, Lu) Topological Kagome Magnets. *Phys. Rev. Lett.* **2021**, *126*, No. 246602.
(27) Weiland, A.; Eddy, L. J.; McCandless, G. T.; Hodovanets, H.; Paglione, J.; Chan, J. Y. Refine Intervention: Characterizing Disordered $Yb_{0.5}Co_3Ge_3$. *Cryst. Growth. Des.* **2020**, *20*, 6715−6721.
(28) Wang, Y.; McCandless, G. T.; Wang, X.; Thanabalasingam, K.; Wu, H.; Bouwmeester, D.; van der Zant, H. S. J.; Ali, M. N.; Chan, J. Y. Electronic Properties and Phase Transition in the Kagome Metal $Yb_{0.5}Co_3Ge_3$. *Chem. Mater.* **2022**, *34*, 7337−7343.
(29) Wang, C.; Liu, S.; Jeon, H.; Jia, Y.; Cho, J.-H. Charge Density Wave and Superconductivity in the Kagome Metal CsV_3Sb_5 Around a Pressure-Induced Quantum Critical Point. *Phys. Rev. Mater.* **2022**, *6*, No. 094801.
(30) Sinha, M.; Vivanco, H. K.; Wan, C.; Siegler, M. A.; Stewart, V. J.; Pogue, E. A.; Pressley, L. A.; Berry, T.; Wang, Z.; Johnson, I.; Chen, M.; Tran, T. T.; Phelan, W. A.; McQueen, T. M. Twisting of 2D Kagomé Sheets in Layered Intermetallics. *ACS Cent. Sci.* **2021**, *7*, 1381−1390.
(31) Avila, M. A.; Takabatake, T.; Takahashi, Y.; Bud'ko, S. L.; Canfield, P. C. Direct Observation of Fe spin Reorientation in Single-Crystalline $YbFe_6Ge_6$. *J. Phys.: Condens. Matter* **2005**, *17*, 6969.
(32) Cadogan, J. M.; Ryan, D. H. A Study on the Magnetic Behaviour of Polymorphic $YbFe_6Ge_6$. *J. Phys.: Condens. Matter* **2010**, *22*, No. 016009.
(33) Canfield, P. C.; Fisk, Z. Growth of Single Crystals From Metallic Fluxes. *Philos. Mag. B* **1992**, *65*, 1117−1123.
(34) Canfield, P. C.; Kong, T.; Kaluarachchi, U. S.; Jo, N. H. Use of Frit-Disc Crucibles for Routine and Exploratory Solution Growth of Single Crystalline Samples. *Philos. Mag.* **2016**, *96*, 84−92.
(35) Krause, L.; Herbst-Irmer, R.; Sheldrick, G. M.; Stalke, D. Comparison of Silver and Molybdenum Microfocus X-ray Sources for Single-Crystal Structure Determination. *J. Appl. Crystallogr.* **2015**, *48*, 3−10.
(36) Sheldrick, G. Crystal Structure Refinement with SHELXL. *Acta Crystallogr. C* **2015**, *71*, 3−8.
(37) Bravo, M.; McCandless, G. T.; Baumbach, R. E.; Wang, Y.; Ali, M. N.; Chan, J. Y. Crystal Growth and Physical Properties of Hybrid CoSn−YCo_6Ge_6 Structure Type $Ln_xCo_3(Ge_{1-y}Sn_y)_3$ (Ln = Y, Gd). *Inorg. Chem.* **2023**, *62*, 18049−18055.
(38) Mazet, T.; Ihou-Mouko, H.; Ryan, D. H.; Voyer, C. J.; Cadogan, J. M.; Malaman, B. Valence Change and Magnetic Order in $YbMn_6Ge_{6-x}Sn_x$. *J. Phys.: Condens. Matter* **2010**, *22*, No. 116005.
(39) Venturini, G. Filling the CoSn Host-Cell: the $HfFe_6Ge_6$-type and the Related Structures. *Z. Kristallogr. - New Cryst. Struct.* **2006**, *221*, 511−520.
(40) Baber, W. G.; Mott, N. F. The Contribution to the Electrical Resistance of Metals from Collisions between Electrons. *Proc. R. Soc. London, Ser. A* **1937**, *158*, 383−396.
(41) Wiser, N. The Electrical Resistivity of the Simple Metals. *Contemporary Physics* **1984**, *25*, 211−249.
(42) Tran, V. H.; Paschen, S.; Rabis, A.; Baenitz, M.; Steglich, F.; du Plessis, P. D. V.; Strydom, A. M. U_2Ru_2Sn: a New Kondo Insulator? *Phys. B* **2002**, *312-313*, 215−217.
(43) Braun, T.; Hlukhyy, V. Structural Order-Disorder in $CaFe_6Ge_6$ and $Ca_{1-x}Co_6Ge_6$. *J. Solid State Chem.* **2023**, *318*, No. 123742.
(44) Welberry, T. R.; Butler, B. D. Diffuse X-ray Scattering from Disordered Crystals. *Chem. Rev.* **1995**, *95*, 2369−2403.
(45) Welberry, T. R.; Weber, T. One Hundred Years of Diffuse Scattering. *Cryst. Rev.* **2016**, *22*, 2−78.
(46) Proffen, T. Analysis of Occupational and Displacive Disorder using the Atomic Pair Distribution Function: A Systematic Investigation. *Z. Kristallogr. - New Cryst. Struct.* **2000**, *215*, 661−668.
(47) Zaharkof, O.; Cervellino, A.; Estermann, M.; Schobinger-Papamantellos, P. Structure of the Microdomain Boundaries in RFe_6Ge_6 (R = Tb, Ho or Er) Crystals from Diffuse X-ray Scattering. *Philos. Mag. A* **2000**, *80*, 27−47.
(48) Oleksyn, O. Y.; Böhm, H. Ordering in $DyFe_6Sn_6$ Studied by Conventional X-ray Single Crystal Diffraction. *Z. Kristallogr. - Cryst. Mater* **1998**, *213*, 270−274.
(49) Fredrickson, D. C.; Lidin, S.; Venturini, G.; Malaman, B.; Christensen, J. Origins of Superstructure Ordering and Incommensurability in Stuffed CoSn-Type Phases. *J. Am. Chem. Soc.* **2008**, *130*, 8195−8214.
(50) Mruz, O. Y.; Starodub, P. K.; Bodak, O. I. New Representatives of the Structure Type YCo_6Ge_6. *Dop. Akad. Nauk Ukrain. RSR* **1984**, *Ser B12*, 45−47.
(51) Venturini, G. Crystallographic and Magnetic Properties of $TbFe_6Ge_{6-x}Ga_x$ Compounds ($0.5 \leq x \leq 3.5$). *J. Alloys Compd.* **2001**, *329*, 8−21.
(52) Ihou-Mouko, H.; Venturini, G. Crystallographic Properties of $ErFe_6Sn_{6-x}Ga_x$ Compounds ($0 < x < 6$). *J. Alloys Compd.* **2005**, *396*, 59−63.
(53) Mazet, T.; Welter, R.; Malaman, B. A Study of the New Ferromagnetic $YbMn_6Sn_6$ Compound by Magnetization and Neutron Diffraction Measurements. *J. Magn. Magn. Mater.* **1999**, *204*, 11−19.
(54) Magnette, A.; Vernière, A.; Venturini, G.; Eichenberger, L.; Malaman, B.; Mazet, T. Crystal and Magnetic Properties of $YbMn_{6-y}Fe_ySn_6$ ($y \leq 1$). *J. Magn. Magn. Mater.* **2018**, *458*, 19−22.
(55) Fedyna, M. F.; Skolozdra, R. V.; Gorelenko, Y. K. Magnetic and electric properties of RCo_6Ge_6 (R = Y, Dy, Er-Lu). *Neorg. Mater.* **1999**, *35*, 461−463.
(56) Cadogan, J. M.; Ryan, D. H. Independent Magnetic Ordering of the Rare-Earth (R) and Fe Sublattices in the RFe_6Ge_6 and RFe_6Sn_6 series. *J. Alloys Compd.* **2001**, *326*, 166−173.
(57) Oleksyn, O.; Schobinger-Papamantellos, P.; Rodríguez-Carvajal, J.; Brück, E.; Buschow, K. H. J. Crystal Structure and Magnetic Ordering in $ErFe_6Ge_6$ studied by X-ray, Neutron Diffraction and Magnetic Measurements. *J. Alloys Compd.* **1997**, *257*, 36−45.
(58) Cadogan, J. M.; Ryan, D. H.; Swainson, I. P. Neutron Diffraction Determination of the Magnetic Structure of $DyFe_6Ge_6$. *J. Phys.: Condens. Matter* **2000**, *12*, 8963.
(59) Schobinger-Papamantellos, P.; Buschow, K. H. J.; de Boer, F. R.; Ritter, C.; Isnard, O.; Fauth, F. The Fe Ordering in RFe_6Ge_6 Compounds with Non-Magnetic R (R = Y, Lu, Hf) Studied by Neutron Diffraction and Magnetic Measurements. *J. Alloys Compd.* **1998**, *267*, 59−65.

https://doi.org/10.1021/acs.chemmater.5c00119
Chem. Mater. 2025, 37, 2302−2313

(60) Häggström, L.; Ericsson, T.; Wäppling, R.; Chandra, K. Studies of the Magnetic Structure of FeSn Using the Mössbauer Effect. *Phys. Scr.* **1975**, *11*, 47−54.
(61) Yang, T.-H.; Gao, S.; Zhang, Y.; Olds, D.; Meier, W. R.; Stone, M. B.; Sales, B. C.; Christianson, A. D.; Zhang, Q. Simultaneous Development of Antiferromagnetism and Local Symmetry Breaking in a Kagome Magnet $(Co_{0.45}Fe_{0.55})Sn$. *J. Am. Chem. Soc.* **2024**, *146*, 34374−34382.
(62) Li, V. M.; Adams, M.; Shatruk, M. Generating Ferromagnetic Kagomé Metal by Magnetic Phase Boundary Mapping in the YFe_6Ge_6−YCo_6Ge_6 System. *Chem. Mater.* **2025**, *37*, 247.

https://doi.org/10.1021/acs.chemmater.5c00119
Chem. Mater. 2025, 37, 2302−2313